JOURNAL OF COMPUTATIONAL PHYSICS 99, 214–232 (1992)

Harmonic Stokes Flow through Periodic Porous Media: a 3D Boundary Element Method

LIONEL BORNE

Institut Franco-Allemand de Recherches de Saint-Louis, 5, rue de l'Industrie, 68301 Saint-Louis Cedex, France

Received December 7, 1989; revised May 9, 1991

Our interest is in dynamic filtration through periodic, porous, saturated media. More precisely, here we develop a three-dimensional numerical model, based on boundary element methods, to compute the dynamic permeability over a wide range of such media. This generalized Darcy coefficient is obtained by the homogenization process applied to a periodic, deformable, porous medium under dynamic solicitations. An unusual choice of Green functions is made. A simple numerical procedure is used for the treatment of the periodic boundary conditions. Recent advances to treat singular integrals are employed and extended to our case. The method is tested on simple examples where theoretical results are available. In the static case results are compared with many previous results on periodic arrays of spheres. New results are given in the dynamic case. The scaling behavior for dynamic permeability in porous media is checked and discussed. © 1992 Academic Press, Inc.

INTRODUCTION

The dynamic behavior of porous saturated media is our field of interest. This concerns many processes and applications, such as flow in porous media (drag forces in packed bed reactors, for instance), propagation of elastic waves (seismic, mechanical) in soils or other porous media, acoustic propagation in marine sediments, etc.

The aim of this paper is to compute the generalized Darcy coefficient. This is an important dynamic parameter governing fluid flow in porous media, indicated by the homogenization process. This method applied to a fine periodic, deformable, saturated, porous medium under dynamic solicitations leads to a macroscopic description and allows us to perform a complete calculation of the effective parameters. The only geometrical restriction on our computation is the spatial periodicity (at the microscopic level). Previous work [3], restrained to the two-dimensional case, underlines the influence of geometry. We now want to test this again on three-dimensional geometries. Moreover, we want to build a numerical tool, capable of dealing with a wide range of geometries. Some existing computations are limited to the static case and to media of a specific nature (periodic array of spheres [35]). Finally, recent numerical [31] and experimental [18] results exhibit a scaling behavior for the dynamic permeability in porous media [32], based on a theoretical study of the limiting cases of low and high frequency response [21]. We will discuss these results.

The first part underlines the main points of the filtration law. The mathematical problem to be solved is introduced. We shall call it periodic (in space), harmonic (in time), Stokes (linear) flow. In a second part, we discuss the choice of a boundary element method for 3D problems and deal with Green kernels. Then the third part deals with our boundary element formulation. Regularization methods for singular integrals are presented. In the next part, we build the discrete problem to be solved and show its implementation. Finally, we present tests, experiments, and we conclude with the scaling behavior for dynamic permeability in porous media.

1. GENERALIZED DARCY PERMEABILITY

The dynamic behavior of fluid-filled porous media was first studied by Biot [8–11]. His theoretical model, applied directly at the macroscopic level, is now generally accepted by scientists. Moreover, his prediction of the existence of a second bulk compressional wave in such media, was confirmed experimentaly later by Plona [27]. Nevertheless, the phenomenological Biot approach does not allow precise computations of the governing coefficients involved in his law. This has led to much work reported by several authors [7, 12, 16, 19, 29, 30, 33, 34].

The homogenization process applied to this problem by Sanchez–Palencia and Auriault [4] overcomes this difficulty and enables us to perform complete computations of the governing parameters. From simple assumptions at the pores scale, this technique yields the macroscopic description and clearly exhibits the parameters involved.

The important point to remember is as follows: The formulation obtained by the homogenization approach is

0021-9991/92 $3.00

similar to Biot results and highlights a generalized (dynamic) Darcy law. Moreover, it underlines the role of this dynamic filtration law, which contains all the dynamic coupling between the two phases (solid–fluid) in the dynamic behavior of deformable saturated porous media [2, 3].

As in the static case, a permeability tensor characterizes this filtration law. We shall call it the generalized Darcy permeability. Furthermore, we obtain the same generalized Darcy law if we consider the dynamic behavior of a fluid-saturated, deformable, porous medium or the dynamic behavior of a fluid flow through a rigid porous medium [2].

In literature, many authors present experiments of waves propagating in deformable, porous, saturated media [7, 29]. All these experiments give encouraging results, but are as yet difficult to carry out and to analyze in detail. Computations, or measurements of the effective parameters of the medium are difficult. The role of the pore structure geometry was introduced in Biot's model using a "tortuosity" coefficient. But how can we determine its possible range of variation?

A previous work [3], detailed in [13], shows in two-dimensional cases, the influence of the geometry on the generalized Darcy coefficient. Moreover, by an asymptotic study at high frequencies, it exhibited interesting geometrical parameters. Consequently, the influence of the pore geometry on wave propagation in saturated porous media have been studied [13, 16, 22, 30]. But these questions need further studies. More recently, some authors have proposed an approximate universal function independent of porous microstructures for the dynamic permeability [32]. After providing new 3D results, we will check and discuss this approximate universal behavior.

To obtain the generalized Darcy coefficient value on true 3D geometries, we need to solve a kind of Navier–Stokes problem with unusual boundary conditions. It is the purpose of our work, but let us first introduce the homogenization process, which will lead us to the problem to be dealt with.

Homogenization Process

Starting from a microscopic description (pore level) of the behavior of the two phases, solid and fluid, the homogenization process leads to an equivalent, homogeneous, macroscopic description of the medium. This homogenization technic uses the so-called double-scale method described in Ref. [6, 28]. A small dimensionless parameter ε, ratio of a characteristic microscopic length and a characteristic macroscopic length, and two dependent spatial variables x and $y = x/\varepsilon$ are used. x and y describe respectively the macroscopic and microscopic situations. Moreover, the micro-structure is assumed to be spatially periodic (for the variable y), which implies the periodicity

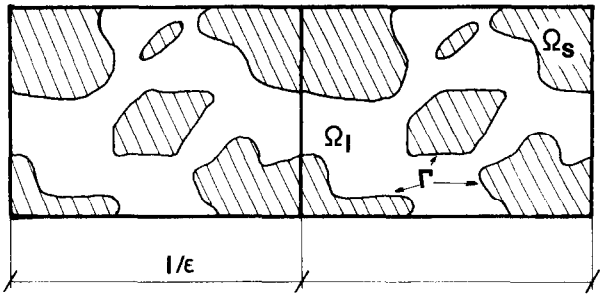

FIG. 1. Two periods of the periodic medium.

for the geometry and the local parameters. In the case of porous media, two periods Ω are sketched in Fig. 1. Then, the equivalent homogeneous situation is given by the asymptotic behavior when ε vanishes. Even when the zero value is not effectively reached in a concrete case, the method leads to a first approximation for the macroscopic equivalent behavior. The heuristic method consists of seeking the unknown in the form $v = v^{(0)}(x, y) + \varepsilon v^{(1)}(x, y) + \varepsilon^2 v^{(2)}(x, y) + \cdots$, where the $v^{(i)}(x, y)$ are periodic in y, by introducing such developments in the equations describing the local behavior, and identifying the powers of ε.

Rigid Porous Medium

Dealing with fluid flow through a rigid porous medium and the following assumptions for the microscopic description, this homogenization process leads to the main following results. Details are available in [1–4, 6].

Microscopic Description: Notations and Assumptions

- The solid part Ω_s is assumed to be rigid.
- The fluid part Ω_l is assumed to be Newtonian and incompressible. The velocity of the fluid is small enough (slow flow) to satisfy linearized Navier–Stokes equations. But the linear dynamic term $(\rho(\partial V/\partial t))$ is taken into account.
- For the sake of simplicity of the study, the motion will be isothermal and monochromatic. Thus we shall use usual complex notations to suppress time derivatives.
- Dealing with porous media, we use a common sign convention for the solid and fluid stresses. They are positive in traction, as usual in solid mechanics. This gives an unconventional sign for fluid pressure.

Homogenization Results

- At the first order, the pressure $p = p^{(0)}(x, y) = p^{(0)}(x)$, is constant over the period. The microscopic pressure $p^{(1)}$, gives the local periodic variations. This natural result for the homogenization process is known to people dealing with flow in periodic arrays [20].

• At the first order, the velocity $v^{(0)} = v^{(0)}(x, y)$ is the solution of the problem

$$\mu' \frac{\partial^2 V_j}{\partial y_k \partial y_k} + \frac{\partial P}{\partial y_j} - i\omega\rho V_j = -F_j \tag{1}$$

$$\frac{\partial V_j}{\partial y_j} = 0$$ with the following boundary conditions:

$$\mathbf{V} = \mathbf{0} \text{ on } \Gamma, \text{ the solid-fluid interfaces;}$$

$$\mathbf{V} \text{ and } P \text{ are } \Omega\text{-periodic, where} \tag{2}$$

ω is the pulsation.

$\mu = \varepsilon^2 \mu'$ is the dynamic viscosity. This scaling is a consequence of the assumptions made on the fluid at the microscopic level (linear (slow) dynamic flow).

ρ denotes the mass per unit of volume.

V_j is the complex amplitude of the velocity component j.

P is the complex amplitude of the microscopic pressure.

F is the macroscopic pressure gradient, constant over the period Ω. $F = \partial p^{(0)}/\partial x$.

The linear problem (1) is a kind of linear Navier–Stokes problem, with a splitting of the pressure gradient in a microscopic part and a macroscopic part F constant over the period, which is the impellar of the flow. It is well defined, with existence and uniqueness of a solution of the form: $V_j = k_{ji}(y, \omega) F_i$ (see [2]).

Integrating over Ω_l, we get the generalized macroscopic Darcy's law. $\langle V_j \rangle = (1/|\Omega|) \int_{\Omega l} V_j \, d\Omega = K_{jl}(\omega) F_l$ with the generalized permeability tensor $K_{jl}(\omega) = (1/|\Omega|) \int_{\Omega l} k_{jl}(y, \omega) \, d\Omega$.

Moreover, the technique employed gives us a clear physical meaning for the macroscopic quantity defined. $\langle V_j \rangle$ is representative of a flux. In a more physical way, we could write: $F_l = H_{lj}(\omega) \langle V_j \rangle$ with $H_{lj}(\omega) = 1/K_{lj}(\omega) = H1_{lj}(\omega) + iH2_{lj}(\omega)$. The real part, $H1_{lj}(\omega)$, is representative of the viscous dissipative energy and the imaginary part, $H2_{lj}(\omega)$, is representative of the inertia terms. The tensor $H(\omega)$ can also be interpreted as a true spectral signature of a porous medium.

Our purpose is to compute $H(\omega)$, for several 3D geometries. Solving numerically the problem (1) (microscopic level, variable y), with boundary conditions (2) will give us the velocity field on the fluid for a given macroscopic pressure gradient F. Then $H(\omega)$ is obtained by averaging the velocities on the fluid domain. Numerically it would be convenient to deal with the equivalent dimensionless problem

$$\frac{1}{2} \frac{\partial^2 V^{(a)}_j}{\partial y^{(a)}_k \partial y^{(a)}_k} - i\omega^{(a)} V^{(a)}_j + \frac{1}{2} \frac{\partial P^{(a)}}{\partial y^{(a)}_j} = -F^{(a)}_j \tag{3}$$

$$\frac{\partial V^{(a)}_j}{\partial y_j} = 0, \qquad \text{and } \mathbf{V}^{(a)} = \mathbf{0} \text{ on } \Gamma;$$

$$\mathbf{V}^{(a)}, P^{(a)} \Omega\text{-periodic.} \tag{4}$$

with the following definitions for the dimensionless quantities with superscript (a):

$y^{(a)}_i = y_i \varepsilon / a$, a is a characteristic length of the pores.

$\omega^{(a)} = \omega a^2 / 2\nu$

$V^{(a)}_k = V^{(0)}_k a / \nu$

$P^{(a)} = P^{(1)} a^2 \varepsilon / \mu\nu$

$F^{(a)}_k = (a^3 / 2\mu\nu)(\partial p^{(0)} / \partial x_k)$.

In the following, we are going to deal only with dimensionless quantities and work at the microscopic level ($y^{(a)}$). Since there is no possible confusion, the super script (a) will be omitted.

2. A BOUNDARY ELEMENT METHOD

Our purpose is now to compute $H(\omega)$ for various three-dimensional cases, using an efficient numerical tool. Let us first answer the following question:

Why do we use a boundary element method?

Let us first recall the following points of the previous 2D finite element model [14, 15]:

• First, to build the mesh we used complex mapping. The domain under consideration was transformed into the unit square. An obvious, uniform mapping was then done with isotropic elements, and, using the inverse transform, the final mesh was obtained. It was very well adapted to our problem, because the lines of the mesh were also the current lines and potential lines of an inviscid flow. For a 3D problem, the extension of this method is not possible. The problem of efficient automatic meshing of various 3D volumes, starting from a boundary mesh, is sometimes difficult, despite recent advances in this area.

• The following point concerns the finite elements available for this kind of problem. Satisfying exactly the incompressibility condition for the fluid is not easy and leads to complicated and expensive elements. To overcome this difficulty, an iterative scheme was used, which partially satisfied this constraint. Moreover, the cheaper conformal element used was quadratic, and our nodal unknown values were and are complex, this leads rapidly to a large problem in terms of memory size and, consequently, computer time. So a suitable refinement in the mesh could become very expensive.

On the other hand, the boundary element method gives a compromise which appears more adapted to solve our 3D linear problem. The main advantages are the following:

- Our purpose is to compute the macroscopic velocity $\langle V_j \rangle$. We shall show that it can be expressed only as a function of boundary integrals. Then only the boundary will be used to build the discrete problem. And so the total number of degrees of freedom is reduced.
- The incompressibility condition is exactly satisfied by way of the Green kernel. The problem will be solved directly.

There are, however, some difficulties to overcome. These will be mentioned and solved in the following. It should be noted here that despite the reduction of the total number of degrees of freedom, the reduction in memory requirements is not so marked. The matrix of the linear system to be solved is full, rather than sparse, and often ill conditioned.

In order to make use of the boundary element method we must first obtain the Green kernel. Starting with the usual Green kernel for the classical Stokes problem [24] and the well-known fundamental singular solution for the periodic Stokes problem [20], we will give two new Green kernels. One will come from a direct extension of the result for the periodic Stokes problem, taking into account the dynamic term. The other one, nonperiodic, will be obtained using the Kupradze [23] method.

2.1. Green kernels

2.1.1. *The Usual Stokes Problem*

For the usual Stokes problem (static), the Green kernel is available in [24] and is recalled:

$$\alpha_j^k = \frac{1}{4\pi}\left(\frac{\delta_{jk}}{|x-y|} + \frac{(x_j-y_j)(x_k-y_k)}{|x-y|^3}\right)$$

$$\text{and} \qquad q^k = \frac{x_k-y_k}{2\pi\,|x-y|^3}.$$

It satisfies

$$\frac{1}{2}\frac{\partial^2 \alpha_j^k}{\partial x_l\,\partial x_l} + \frac{1}{2}\frac{\partial q^k}{\partial x_j} = -\delta_{jk}\delta(x-y) \qquad \text{and} \qquad \frac{\partial \alpha_j^k}{\partial x_j} = 0,$$

where

x is the current point, y is the singular point,

$\delta(x-y)$ is the Dirac distribution at point y,

δ_{jk} is the usual Kronecker symbol,

α_j^k is the velocity component j for a dirac source in direction k,

q^k is the pressure for a dirac source in direction k.

2.1.2. *The Periodic Stokes Problem*

The Dirac source at point y is now replaced by a set of Dirac sources at $\mathbf{y}_m = \mathbf{y} + m_1\mathbf{d}_1 + m_2\mathbf{d}_2 + m_3\mathbf{d}_3$; $m_i \in Z$. $\mathbf{d}_1, \mathbf{d}_2, \mathbf{d}_3$ are the basic vectors defining a unit cell Ω of the periodic array. This leads to the problem:

$$\frac{1}{2}\frac{\partial^2 \alpha_j^k}{\partial x_l\,\partial x_l} + \frac{1}{2}\frac{\partial q^k}{\partial x_j} = -\delta_{kj}\sum_{m_1}\sum_{m_2}\sum_{m_3}\delta(x-y_m) \text{ and } \frac{\partial \alpha_j^k}{\partial x_j} = 0.$$

Hasimoto [20] gave the solutions using Fourier series and $\mathbf{b}_1, \mathbf{b}_2, \mathbf{b}_3$ the usual vectors of the reciprocal lattice. Choosing a zero mean value on Ω for the velocity, the solutions are:

$$\alpha_j^l = \frac{1}{2\pi^2\,|\Omega|}\sum_{|\mathbf{K}|\neq 0}\frac{\delta_{jl} - (K_jK_l/K_mK_m)}{K_mK_m}\,e^{-2i\pi\mathbf{K}\cdot\mathbf{r}}$$

and

$$q^l = -\frac{2}{|\Omega|}(x_l - y_l) - \frac{1}{\pi\,|\Omega|}\sum_{|\mathbf{K}|\neq 0}\frac{iK_l}{K_mK_m}\,e^{-2i\pi\mathbf{K}\cdot\mathbf{r}}$$

with $\mathbf{K} = m_1\mathbf{b}_1 + m_2\mathbf{b}_2 + m_3\mathbf{b}_3$, $m_i \in Z$, and $\mathbf{r} = \mathbf{x} - \mathbf{y}$.

2.1.3. *A Periodic Kernel for Our Periodic, Harmonic Stokes Problem*

With the same notations, and dealing with complex amplitude for our dynamic study, the problem now is:

$$\frac{1}{2}\frac{\partial^2 \alpha_j^k}{\partial x_l\,\partial x_l} + \frac{1}{2}\frac{\partial q^k}{\partial x_j} - i\omega\alpha_j^k = -\delta_{kj}\sum_{m_1}\sum_{m_2}\sum_{m_3}\delta(x-y_m) \text{ and } \frac{\partial \alpha_j^k}{\partial x_j} = 0.$$

Using Fourier series we obtain

$$\alpha_j^l = \frac{1}{2\pi^2\,|\Omega|}\sum_{|\mathbf{K}|\neq 0}\frac{\delta_{jl} - (K_jK_l/K_mK_m)}{K_mK_m + (i\omega/2\pi^2)}\,e^{-2i\pi\mathbf{K}\cdot\mathbf{r}}$$

and

$$q^l = -\frac{2}{|\Omega|}(x_l - y_l) - \frac{1}{\pi\,|\Omega|}\sum_{|\mathbf{K}|\neq 0}\frac{iK_l}{K_mK_m}\,e^{-2i\pi\mathbf{K}\cdot\mathbf{r}},$$

where q^l is the same as for $\omega = 0$. We will come back later to this property.

Direct numerical use of these kernels (singular Fourier series) by way of a collocation method will lead to unreasonable computations. In the static case (Stokes flow), Zick and Homsy [35], dealing with periodic arrays of spheres, overcame the difficulty by using a Galerkin method over a set of spherical harmonic functions, forming a complete set over the surface of a sphere. This allowed them to perform analytic integrations and to obtain reasonable series to compute.

For our dynamic linear periodic Stokes problem, the singular Fourier series are very similar to those of the usual Stokes problem. From a computational viewpoint, tests have shown that the velocity series become more and more expensive to evaluate when ω is increasing. Moreover, in order to deal with a wide range of geometries, we do not wish to use a set of spherical harmonic functions, but rather to use a finite element approximation to solve our boundary integral problem.

We shall now overcome the difficulty of evaluating such Fourier series by using a fundamental singular solution not Ω periodic. The periodic boundary conditions will then be satisfied by the same numerical trick used in [14] for the 2D finite element model.

Unfortunately, this solution leads us to deal with all the boundaries, not just the solid–fluid interface. For simple cubic packing of spheres, for instance, it means that a new and different mesh must be used for each different concentration. But from a practical point of view, is the same mesh of the solid–fluid interface (which stays the same for different concentrations) convenient to reach accurate results over all the range of concentrations? Flows do not remain identical around the spheres.

2.1.4. *A Nonperiodic Kernel for Our Periodic, Harmonic Stokes Problem*

With the previous notations, our purpose is now to find α_j^k and q^k such that:

$$\frac{1}{2}\frac{\partial^2 \alpha_j^k}{\partial x_l \partial x_l} + \frac{1}{2}\frac{\partial q^k}{\partial x_j} - i\omega\alpha_j^k = -\delta_{kj}\delta(x-y) \quad \text{and} \quad \frac{\partial \alpha_j^k}{\partial x_j} = 0.$$

To summarize the Kupradze method [23], which will give us a solution:

The general problem to solve can be written: $\mathbf{B}\cdot\mathbf{G} + \delta\cdot\mathbf{I} = 0$, where

$\mathbf{I}$ is the unit matrix,

$\mathbf{G}$ is the Green matrix, which gives the set of Green kernel,

$\mathbf{B}$ is a matrix operator,

δ is the Dirac distribution at the origin.

If $\times$ denotes the convolution product, in terms of distributions, then: $[\mathbf{B}\cdot\delta\mathbf{I}]\times\mathbf{G} + \delta\cdot\mathbf{I} = 0$. So $\mathbf{G}$ appears to be the inverse for the convolution product of $[\mathbf{B}\cdot\delta\mathbf{I}]$. We define now the set of distributions $[\mathbf{B}'\cdot\delta\mathbf{I}]$ so that $[\mathbf{B}\cdot\delta\mathbf{I}]\times[\mathbf{B}'\cdot\delta\mathbf{I}] = [\det\mathbf{B}\cdot\delta\mathbf{I}]$. (Note, that the matricial operator $[\mathbf{B}']$ is easy to build using the cofactor of $[\mathbf{B}]$.)

If ϕ is the scalar field solution of $(\det\mathbf{B}\cdot\delta)\times\phi + \delta = 0$, ϕ is also solution of $[\det\mathbf{B}\cdot\delta\mathbf{I}]\times\phi\mathbf{I} + \delta\mathbf{I} = 0$. Consequently $[\mathbf{B}\delta\mathbf{I}\times\mathbf{B}'\delta\mathbf{I}]\times\phi\mathbf{I} + \delta\mathbf{I} = 0$, and therefore $\mathbf{G} = [\mathbf{B}'\delta\mathbf{I}]\times\phi\mathbf{I}$ or $\mathbf{G} = \mathbf{B}'(\phi\mathbf{I})$. The problem is then reduced to finding the scalar solution ϕ. We will now solve it for our case.

Using i as the pure imaginary number and Δ as the usual Laplacian operator, we obtain for our problem,

$$\mathbf{B} = \begin{bmatrix} \frac{1}{2}\Delta - i\omega & 0 & 0 & \frac{1}{2}\frac{\partial}{\partial x_1} \\ 0 & \frac{1}{2}\Delta - i\omega & 0 & \frac{1}{2}\frac{\partial}{\partial x_2} \\ 0 & 0 & \frac{1}{2}\Delta - i\omega & \frac{1}{2}\frac{\partial}{\partial x_3} \\ \frac{1}{2}\frac{\partial}{\partial x_1} & \frac{1}{2}\frac{\partial}{\partial x_2} & \frac{1}{2}\frac{\partial}{\partial x_3} & 0 \end{bmatrix}$$

$$\det\mathbf{B} = \left(\tfrac{1}{2}\Delta - i\omega\right)\left(\tfrac{1}{2}\Delta - i\omega\right)\left(-\tfrac{1}{4}\Delta\right)$$

$$\mathbf{B}' = \frac{1}{2}\left(\frac{1}{2}\Delta - i\omega\right)\begin{bmatrix} \frac{1}{2}\left(\frac{\partial^2}{\partial x_1\partial x_1} - \Delta\right) & \frac{1}{2}\frac{\partial^2}{\partial x_2\partial x_1} & \frac{1}{2}\frac{\partial^2}{\partial x_3\partial x_1} & -\frac{\partial}{\partial x_1}\left(\frac{1}{2}\Delta - i\omega\right) \\ \frac{1}{2}\frac{\partial^2}{\partial x_1\partial x_2} & \frac{1}{2}\left(\frac{\partial^2}{\partial x_2\partial x_2} - \Delta\right) & \frac{1}{2}\frac{\partial^2}{\partial x_3\partial x_2} & -\frac{\partial}{\partial x_2}\left(\frac{1}{2}\Delta - i\omega\right) \\ \frac{1}{2}\frac{\partial^2}{\partial x_1\partial x_3} & \frac{1}{2}\frac{\partial^2}{\partial x_2\partial x_3} & \frac{1}{2}\left(\frac{\partial^2}{\partial x_3\partial x_3} - \Delta\right) & -\frac{\partial}{\partial x_3}\left(\frac{1}{2}\Delta - i\omega\right) \\ -\frac{\partial}{\partial x_1}\left(\frac{1}{2}\Delta - i\omega\right) & -\frac{\partial}{\partial x_2}\left(\frac{1}{2}\Delta - i\omega\right) & -\frac{\partial}{\partial x_3}\left(\frac{1}{2}\Delta - i\omega\right) & 2\left(\frac{1}{2}\Delta - i\omega\right)\left(\frac{1}{2}\Delta - i\omega\right) \end{bmatrix},$$

where ϕ is given by $\left(-\tfrac{1}{4}\Delta\right)\left(\tfrac{1}{2}\Delta - i\omega\right)\left(\tfrac{1}{2}\Delta - i\omega\right)\phi + \delta = 0$.

Using $\psi = \left(\tfrac{1}{2}\Delta - i\omega\right)\phi$, it becomes $\left(-\tfrac{1}{4}\Delta\right)\left(\tfrac{1}{2}\Delta - i\omega\right)\psi + \delta = 0$. Naturally, we search ψ as: $\psi = \alpha_1\cdot\psi_1 + \alpha_2\cdot\psi_2$ with $\alpha_1, \alpha_2 \in R$ and

ψ_1, the well-known solution of $\Delta\psi_1 = \delta$ (Laplace equation) $\cdot\ \psi_1 = -1/4\pi r$ (a nonpropagative wave).

ψ_2, well-known solution of $\Delta\psi_2 - 2i\omega\psi_2 = \delta$ (Helmoltz equation). $\psi_2 = -(1/4\pi r)\, e^{(1+i)\sqrt{\omega}r}$ (a propagative wave attenuated as $\sqrt{\omega}$).

This leads us to

$$\psi = \frac{1}{i\omega\pi r}\left(1 - e^{(1+i)\sqrt{\omega}r}\right)$$

$$G = \frac{1}{4}\begin{bmatrix} \dfrac{\partial^2\psi}{\partial x_1\,\partial x_1} - \Delta\psi & \dfrac{\partial^2\psi}{\partial x_2\,\partial x_1} & \dfrac{\partial^2\psi}{\partial x_3\,\partial x_1} & -\dfrac{\partial}{\partial x_1}(\Delta - 2i\omega)\psi \\ \dfrac{\partial^2\psi}{\partial x_1\,\partial x_2} & \dfrac{\partial^2\psi}{\partial x_2\,\partial x_2} - \Delta\psi & \dfrac{\partial^2\psi}{\partial x_3\,\partial x_2} & -\dfrac{\partial}{\partial x_2}(\Delta - 2i\omega)\psi \\ \dfrac{\partial^2\psi}{\partial x_1\,\partial x_3} & \dfrac{\partial^2\psi}{\partial x_2\,\partial x_3} & \dfrac{\partial^2\psi}{\partial x_3\,\partial x_3} - \Delta\psi & -\dfrac{\partial}{\partial x_3}(\Delta - 2i\omega)\psi \\ -\dfrac{\partial}{\partial x_1}(\Delta - 2i\omega)\psi & -\dfrac{\partial}{\partial x_2}(\Delta - 2i\omega)\psi & -\dfrac{\partial}{\partial x_3}(\Delta - 2i\omega)\psi & \left(\dfrac{1}{2}\Delta - i\omega\right)\left(\dfrac{1}{2}\Delta - i\omega\right)\psi \end{bmatrix}.$$

Let us now give a physical interpretation to this Green matrix.

Naturally, the Green matrix gives the responses of an infinite medium for four independent local sources. These are the four columns of the matrix, which give the three components of the velocity (lines 1, 2, and 3) and the pressure (line 4). The first columns, 1, 2, and 3, correspond to a local harmonic unit force respectively in directions 1, 2, and 3. The column 4 represents a harmonic local volume source.

If α_j^k denotes the velocity component j and q^k denotes the pressure, corresponding to a harmonic local unit volume force in the direction k, we have: $\alpha_j^k = \frac{1}{4}((\partial^2\psi/\partial x_j\,\partial x_k) - \delta_{jk}\,\Delta\psi)$. And using the properties of ψ_1 and ψ_2: $q^k = (\partial/\partial x_k)(1/2\pi r)$. The pressure wave is nonpropagative. This is a diffusive wave. A natural result for the pressure is an isotropic stress in a viscous incompressible fluid. The velocity wave is constituted of two parts:

— a diffusive wave, linked with the pressure wave;

— a propagative and attenuated wave, to link with the deviate part of the loading. The attenuation is the result of viscous dissipation and is proportional to $\sqrt{\omega}$.

In the case of a volume source (column 4) both velocity and pressure waves are diffusive, which is a consequence of the isotropic loading. In order to solve our problem with the macroscopic pressure gradient, we will not use this last kind of volume source.

2.2. The Boundary Element Formulation

2.2.1. *Usual Approach*

Let us now exhibit the boundary element formulation of the problem. First, it will be more convenient to define some new notations. They are as follows: In the fundamental problem the Green pressure q^k will be replaced by the Green stress: $\sigma_{jl}^k = (\partial\alpha_j^k/\partial x_l + \partial\alpha_l^k/\partial x_j) + \delta_{jl}q^k$ and so, our fundamental problem becomes

$$\frac{1}{2}\frac{\partial\sigma_{jl}^k}{\partial x_l} - i\omega\alpha_j^k = -\delta_{kj}\delta(x-y) \tag{5}$$

and

$$\frac{1}{2}\frac{\partial\alpha_j^k}{\partial x_j} = 0. \tag{6}$$

In the same way, using the following dimensionless fluid stress $\Sigma_{jl} = (\partial V_j/\partial x_l + \partial V_l/\partial x_j) + \delta_{jl}P$, the problem to be solved becomes

$$\frac{1}{2}\frac{\partial\Sigma_{jl}}{\partial x_l} - i\omega V_j = -F_j \tag{7}$$

and

$$\frac{1}{2}\frac{\partial V_j}{\partial x_j} = 0 \qquad \text{with} \quad V_j, \Sigma_{jl}\ \Omega\text{-periodic}$$
$$\text{and } V_j = 0 \text{ on } \Gamma. \tag{8}$$

As is customary, to start with the boundary element (B.E.) formulation, we multiply (5) by V_j and (7) by α_j^k and we substract both equations so obtained. Then, by integrating over the fluid part Ω_l of the period Ω, we have

$$\frac{1}{2}\int_{\Omega_l}\left(\frac{\partial\sigma_{jl}^k}{\partial x_l}V_j - \frac{\partial\Sigma_{jl}}{\partial x_l}\alpha_j^k\right)d\Omega = \int_{\Omega_l}(F_j\alpha_j^k - \delta_{kj}\,\delta(x-y)\,V_j)\,d\Omega.$$

Integrating by parts and using Eq. (6) and (8), we obtain the integral equation:

$$\frac{1}{2}\int_{\Omega_l}\frac{\partial}{\partial x_l}(\sigma_{jl}^k V_j - \alpha_j^k\,\Sigma_{jl})\,d\Omega = \int_{\Omega_l}(F_j\alpha_j^k - \delta_{kj}\,\delta(x-y)\,V_j)\,d\Omega \tag{9}$$

The macroscopic pressure gradient, F, is constant over the period Ω, and using the divergence theorem, it follows:

$$\tfrac{1}{2}\int_{\partial\Omega_l}(\sigma_{jl}^k V_j - \alpha_j^k \Sigma_{jl})\, n_l\, d\Gamma = F_j \int_{\Omega_l} \alpha_j^k\, d\Omega - \delta_{kj}\int_{\Omega_l}\delta(x-y)\, V_j\, d\Omega. \quad (10)$$

Let us now change $\int_{\Omega_l}\alpha_j^k\, d\Omega$ into a boundary integral.

2.2.2. *How to Obtain a Boundary Element Formulation*

Integrating (5) over Ω_l allows the previous volume integral to be written for $\omega \neq 0$ in terms of boundary integral. Also making use of the divergence theorem we obtain

$$i\omega\int_{\Omega_l}\alpha_j^k\, d\Omega = \tfrac{1}{2}\int_{\partial\Omega_l}\sigma_{jl}^k n_l\, d\Gamma + \delta_{kj}\int_{\Omega_l}\delta(x-y)\, d\Omega. \quad (11)$$

This method is of interest in saving computational time as shown here below, but becomes numerically more and more ill conditioned as ω decreases.

Another trick, which now works also in the static case, is the following: F_j is constant over Ω_l, so we can write: $F_j = (\partial/\partial x_j)(F_l x_l)$ and then

$$F_j\int_{\Omega_l}\alpha_j^k\, d\Omega = \int_{\Omega_l}\frac{\partial}{\partial x_j}(F_l x_l)\,\alpha_j^k\, d\Omega.$$

Integrating the left-hand side by parts and using the incompressibility we obtain

$$F_j\int_{\Omega_l}\alpha_j^k\, d\Omega = \int_{\Omega_l}\frac{\partial}{\partial x_j}(F_l x_l \alpha_j^k)\, d\Omega$$

and, finally,

$$F_j\int_{\Omega_l}\alpha_j^k\, d\Omega = F_l\int_{\partial\Omega_l}(x_l\alpha_j^k)\, n_j\, d\Gamma. \quad (12)$$

Substituting (12) or (11) in (10) will give the boundary element formulation.

2.2.3. *Regularization of Our Integral Equation*

Singularities in the previous formulation lead to well-known difficulties for numerical computations. Let us try to regularize this equation. The method employed is the direct extension of a regularization technique used for elastostatics and steady state elastodynamics presented in [17]. This is allowed by a property of our Green kernel.

A local study around the singular point y of our non-periodic harmonic Green kernel gives us the following important property:

$$\alpha_j^k(\omega) = \alpha_j^k(\omega=0) + \text{regular terms} \quad (13)$$

$$t_j^k(\omega) = t_j^k(\omega=0) + \text{regular terms} \quad (14)$$

$$(t_j^k = \sigma_{jl}^k n_l).$$

Using (14), we can now obtain a regularized form of our boundary element formulation. Let us consider a rigid body motion of the two phases. It implies: $\Sigma_{jl}=0$; $F_j=0$; $V_j(x)=V_j(y)=\text{const}$. So (10) becomes

$$\tfrac{1}{2}\int_{\partial\Omega_l} t_j^k(\omega=0)\, V_j(y)\, d\Gamma = -\delta_{kj}\int_{\Omega_l}\delta(x-y)\, V_j(y)\, d\Omega. \quad (15)$$

Finally, (10)–(15) lead to the following regularized formulation:

$$\tfrac{1}{2}\int_{\partial\Omega_l}(t_j^k(\omega)-t_j^k(\omega=0))\, V_j(y)\, d\Gamma + \tfrac{1}{2}\int_{\partial\Omega_l} t_j^k(\omega)(V_j - V_j(y))\, d\Gamma - \tfrac{1}{2}\int_{\partial\Omega_l}\alpha_j^k(\omega)\, T_j\, d\Gamma = F_j\int_{\Omega_l}\alpha_j^k(\omega)\, d\Omega \quad (16)$$

$$(T_j = \Sigma_{jl} n_l).$$

The first integral of the left-hand side term is then regular. All the others integrals are now weakly singular $(1/r)$. Numerical evaluation of such weakly singular integrals will be given here below. The highest order of singularity is reduced from $(1/r^2)$ to $(1/r)$. We have already seen how to deal with the right-hand side term, both in static and dynamic cases, but let us underline the following point.

In the dynamic case, (11) can also be regularized. Using (15) it follows:

$$i\omega\int_{\Omega_l}\alpha_j^k(\omega)\, d\Omega = \tfrac{1}{2}\int_{\partial\Omega_l}(t_j^k(\omega)-t_j^k(\omega=0))\, d\Gamma.$$

Please note that here we find, in the right-hand side, the first integral of (16), since $V_j(y)$ can be put out of the integral. Before going on to the discrete problem and its numerical implementation we need to deal with the mean velocity $\langle V_j\rangle$, the true quantity we want to compute,

$$\langle V_j\rangle = \frac{1}{|\Omega|}\int_{\Omega_l} V_j\, d\Omega.$$

2.2.4. *The Stress Method*

Integrating (7) over Ω_l gives

$$\langle V_j \rangle = \frac{1}{2i\omega\,|\Omega|}\int_{\partial\Omega_l} T_j\,d\Gamma + \frac{nF_j}{i\omega},$$

where $n = \dfrac{|\Omega_l|}{|\Omega|}$ is the porosity.

But for $\omega = 0$, this method fails. It just allows us to check the accuracy of our results, $((1/2\,|\Omega|)\int_{\partial\Omega_l} T_j\,d\Omega + nF_j = 0)$. To find a more general method, we must use the velocities computed on the boundary.

2.2.5. *The Velocity Method*

The basic idea we use now is a property of $\langle V_j \rangle$ given by the homogenisation process; it is a flux. From the incompressibility, we deduce the relation $(\partial/\partial x_k)(V_k x_j) = V_j$. Integrating over Ω_l, and using Green's formula, it follows: $\langle V_j \rangle = (1/|\Omega|)\int_{\partial\Omega_l} V_k x_j n_k\,d\Gamma$.

If I_j and S_j denote respectively the length in direction j and the section orthogonal to the direction j of the parallelepipedic period, at $x_j = I_j$ we can write: $\langle V_j \rangle = (1/S_j)\int_{x_j = I_j} V_k n_k\,d\Gamma$.

From a practical point of view, we are going to see the interest and the complementarity of both methods later on.

3. DISCRETE PROBLEM AND NUMERICAL IMPLEMENTATION

3.1. Discrete Problem

We present here a first attempt, so we have made some choices to reach a reasonable precision, at the lowest cost. The results will or will not confirm our choices.

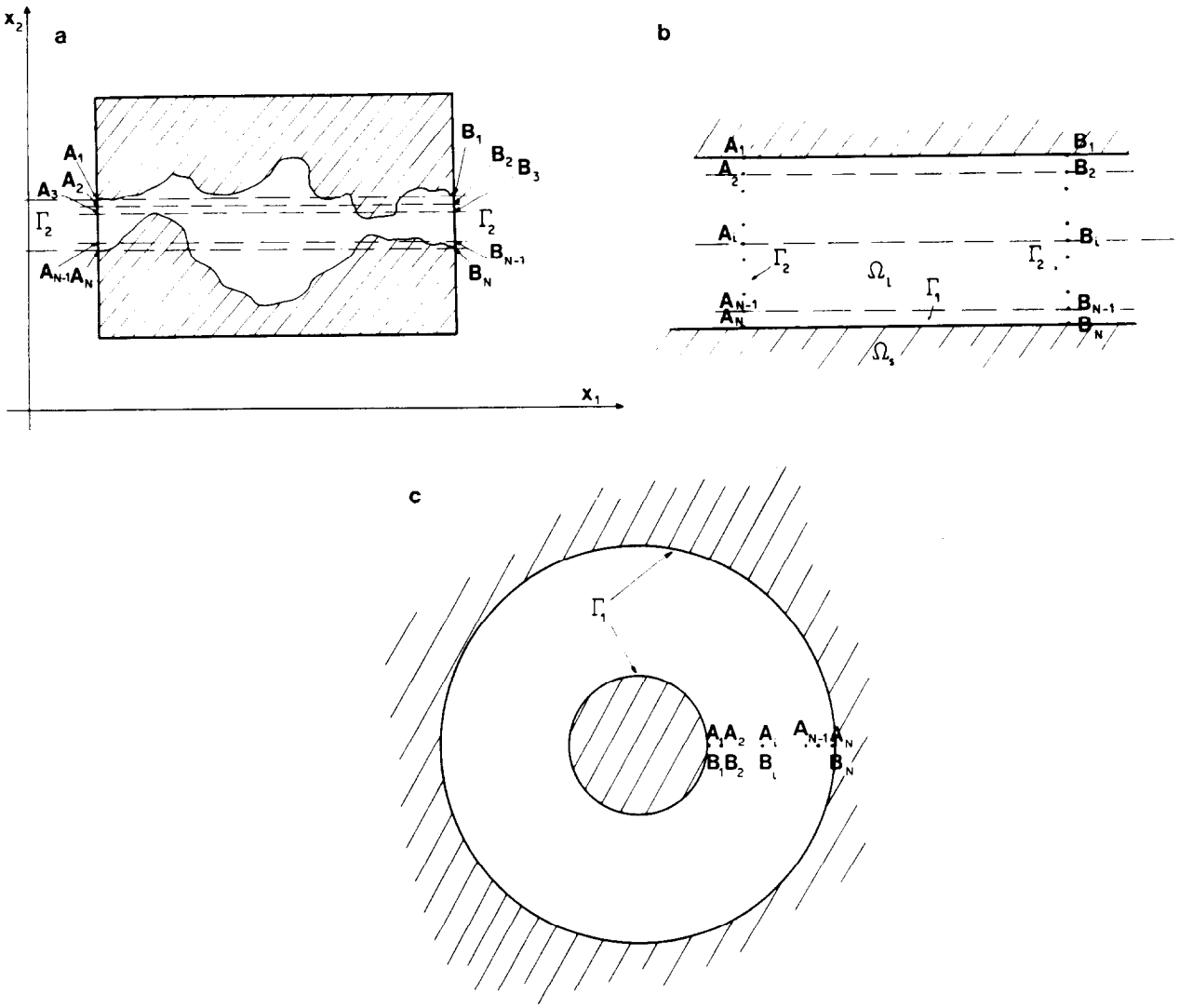

FIG. 2. The periodic boundary conditions in the case of a narrow slit: (a) the periodicity of the nodes, for $i = 1$ to N; $x_2(A_i) = x_2(B_i)$; (b) the case of the narrow slit; (c) The equivalent numerical picture of the narrow slit.

The boundary is approximated by a set Γ_h of usual finite elements. Quadratic elements have been selected to deal with curved surfaces. They are the six-node triangular element and the eight-node quadrilateral element. For the sake of simple implementation, we use constant approximated fields on each finite element, for both stresses and velocities.

3.2. Boundary Conditions

The boundary condition $\mathbf{V} = \mathbf{0}$ on Γ, the solid–fluid interface, is satisfied directly by the formulation. This allows us to perform some integrations only on part of the boundary. For the periodic boundary condition, it is done by using a simple numerical trick as shown by Fig. 2.

First we assume the periodicity of the mesh. Then we assume the same memory location for the nodal unknown vectors (stress and velocity) of two periodic elements. This allows us to save memory and consequently CPU time and leads us to solve a square linear system.

2.3. Integration

Now to build the linear system to solve, we only need to perform integrations. Quadratic elements and kernels do not allow us to perform analytic integrations. Regular integrals are computed using standard numerical integration schemes (Gauss quadrature). Difficulties arise with singular integrals. They are all weakly singular $1/r$. The method employed is presented in detail in [25]. It uses triangle polar-coordinates to reduce the order of singularity by one degree. So we will obtain regular integrals.

Main steps of this singular integration.

• Mapping the curved element into the usual reference plane element using the well-known shape functions.

constant approximated fields on each element, we need one node to compute this constant value. It is chosen as the barycenter of the element. This is also what we call the singular point. In order to obtain triangle with the singular point located on a vertex we split the element into suitable triangles.

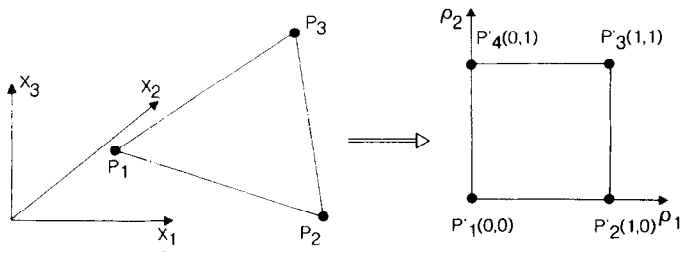

FIG. 3. Regularizing mapping using triangle polar coordinates.

• Regularizing mapping of each of the previous singular triangles. The idea is to map a triangle on a square, so that the singular point located on a vertex of the triangle is mapped onto an edge of the square. According to Fig. 3, the following relations define this regularizing mapping:

$$x_i = (1-\rho_1)\, x_i^{(1)} + \rho_1(1-\rho_2)\, x_i^{(2)} + \rho_1\rho_2 x_i^{(3)}$$

for $i = 1, 2$,

ρ_1, ρ_2 denote point coordinates in the square,

x_i denotes the point coordinate in the triangle,

$x_i^{(j)}$ denotes coordinate i of the vertex j of the triangle.

• Regular integration using Gauss quadrature.

Tests have been performed and give accurate results with a relatively low number of integration points as shown in [25].

3.4. Implementation

In this last section, we briefly describe how we have solved the linear system. Its matrix is full, in general non-symmetric, and could be ill-conditioned. To build a robust and efficient tool, we have selected Gauss elimination as a direct method, with a partial pivot selection strategy. To manage the memory and save CPU time, we have used a dynamic memory management package. This also provides us some minor advantages in the flexibility of our program.

4. TESTS AND EXPERIMENTS

For all the cases with which we want to deal, eigen vectors and eigen values of the second-order tensor H are obvious. In the following, $H(\omega)$ will denote the eigen value sponding eigen direction).

Using the previous dimensionless quantities $\omega^{(a)}$ and $H^{(a)}(\omega) = na^2 H(\omega)/2\mu$ (n is the porosity) (split in real $H1^{(a)}(\omega)$ and imaginary $H2^{(a)}(\omega)$ part) is not a convienent way to plot our results because of the a parameter. We will use a more physical way, as done by Boutin [16]. He uses a characteristic pulsation $\omega_c = nH(\omega = 0)/\rho$, such that both viscous and inertia terms in the flow would be of the same order of magnitude. It is implied with our notations $\omega_c^{(a)} = H1^{(a)}(\omega = 0) = H^{(a)}(\omega = 0)$. Moreover, $nH2/\omega\rho = H2^{(a)}/\omega^{(a)}$ underlines $nH2/\omega$ as a coupling mass of physical interest, which appears in the equations of motion. So our results will be given by two kinds of curves: $H1(\omega)/H1(\omega = 0)$ against ω/ω_c and $nH2(\omega)/\omega\rho$ against ω/ω_c. These are the physical parameters of interest for wave propagation in saturated porous media. This will show how the scaling behavior proposed in [32] is accurate.

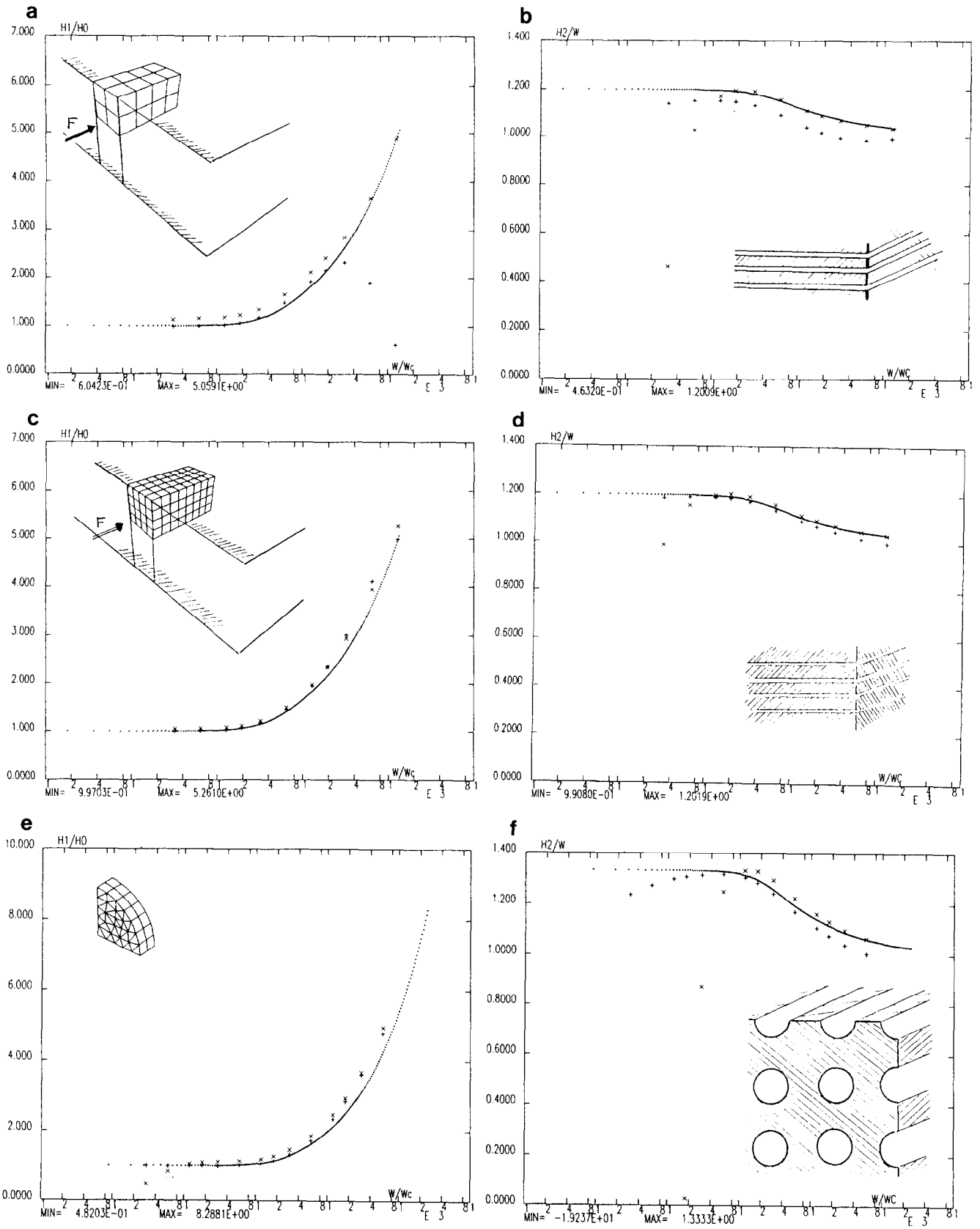

FIG. 4. Dynamic permability for very smooth geometries: +, velocity method; ×, stress method; ·, analytical results. (a)–(d), periodic array of narrow slits; (e), (f), periodic array of cylindrical ducts.

4.1. Tests

Two kinds of tests have been performed: First on smooth geometries where analytical solutions are available; second, on more severe geometries where previous numerical or experimental results are available.

4.1.1. *On Smooth Geometries*

These are periodic arrays made of parallel narrow slits or cylindrical ducts. Analytical results are known [5, 13]. The computation performed is illustrated on each figure by a sketch of the array, a drawing of the period used, its mesh, and an arrow showing the direction of the macroscopic pressure gradient **F**.

Dealing with parallel narrow slits, Fig. 4a–d show the convergence of velocity and stress results towards the numerical solution with grid refinement. The convergence towards the analytical solution is also improved.

Some divergences occur at high and low frequencies; we will come back later on with more severe geometries. Cylindrical ducts (Fig. 4e, f) introduce a new approximation. Our quadratic elements do not exactly map the curved boundary surfaces. So for about the same grid refinement, the results are less accurate than for narrow slits.

Nevertheless, we obtain, not perfect but, good results with the simplest approximation (constant stress and velocity on each element) with relatively coarse mesh and, therefore, at very low cost. For the narrow slits, previous 2D finite element computations [14, 15] have been more expensive. This would allow us to investigate more severe 3D geometries with finer grids at reasonable cost.

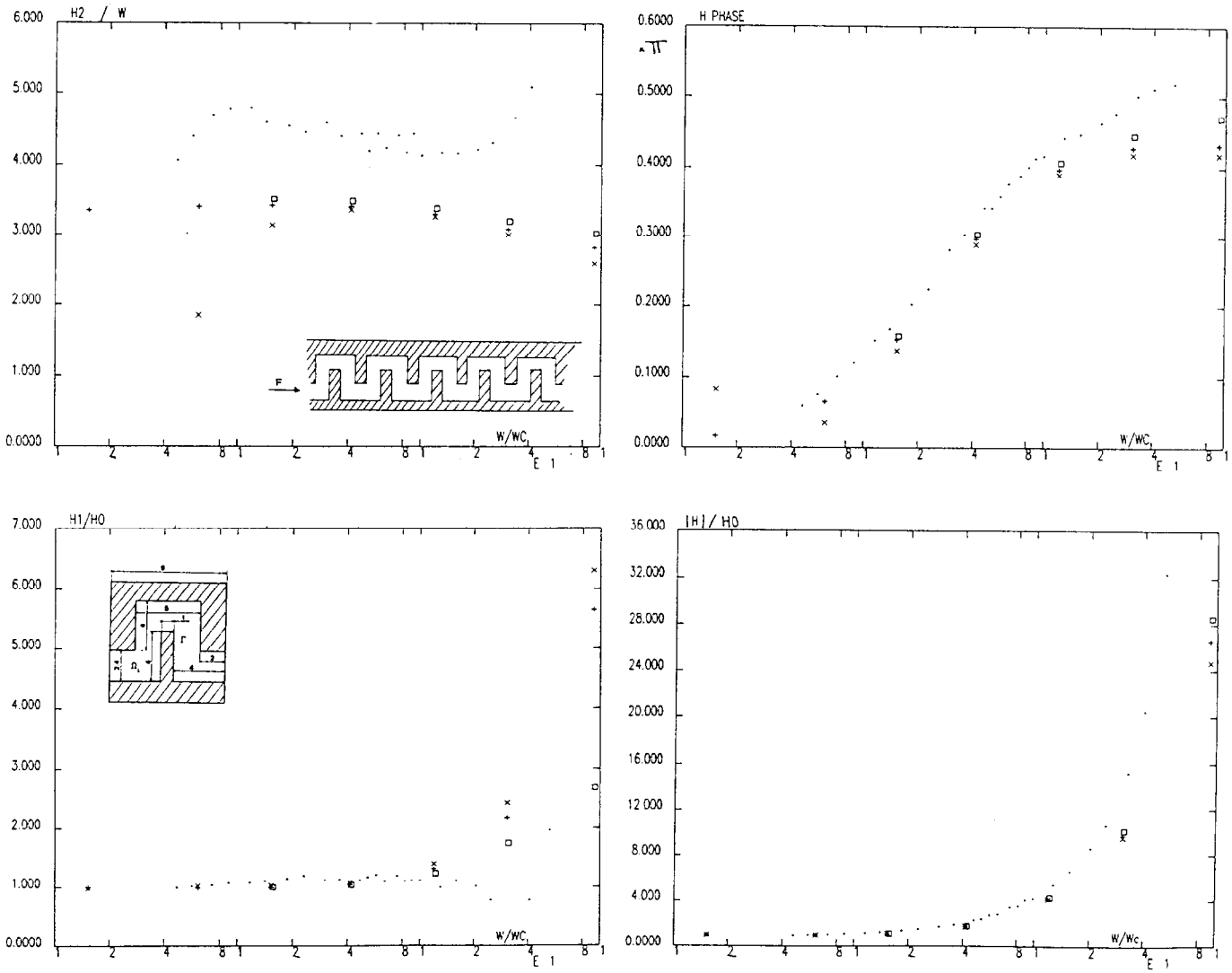

FIG. 5. A more severe 2D example: +, velocity method; ×, stress method; □, previous FEM results; ·, previous experimental results.

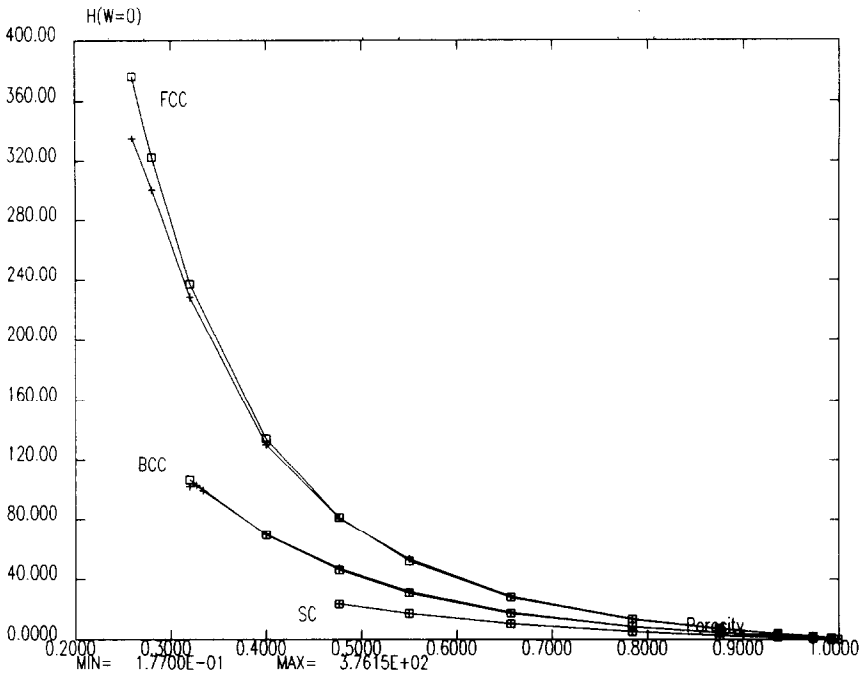

FIG. 6. Static results on three kinds of isotropic arrays of spheres and for various porosity: simple cubic packing, SC; body centred cubic packing, BCC; faced centred cubic packing, FCC; □, existing results; +, velocity method.

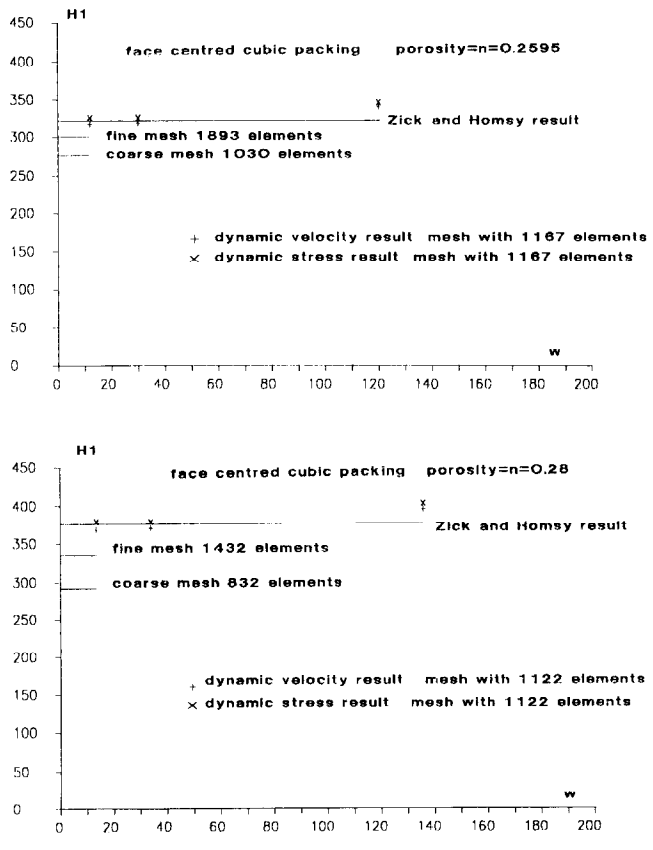

FIG. 7. Accuracy of our static results for FCC array and low porosity values; —, static results; +, dynamic velocity results for low frequencies; ×, dynamic stress results for low frequencies.

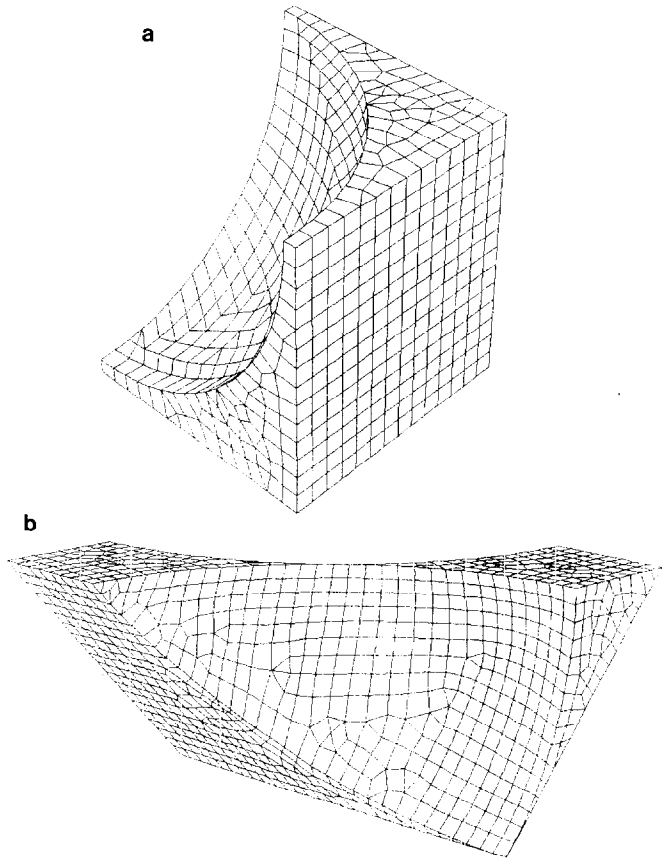

FIG. 8. Two typical meshes for periodic arrays of spheres. All the possible symmetries are used: a. SC array porosity = 0.55 1038 elements; b. FCC array porosity = 0.2595 1432 elements.

4.1.2. *On More Severe Geometries*

These are 3D periodic arrays of spheres [35]; we have studied a 2D example before [3, 13]. For the 2D example (Fig. 5), we check our results with previous numerical and experimental data. $H = H1 + iH2$ can also be written $H = |H|\, e^{i\phi}$. Indeed, $|H|$ and ϕ are the true experimental measurements. Plotting both $|H|$ and ϕ against the pulsation ω will be of interest. Our new results show a good agreement with the low-frequency finite element results. They confirm the problem of the accuracy of the phase measurements. For the high frequency range, these new results improve the old one. They have been checked on several grids; previous finite element results have not. Moreover, experimental high frequency points are difficult to obtain for technical reasons, and so our previous results [3] are suspicious and inaccurate.

Three kinds of isotropic periodic arrays of spheres have been considered, over a wide range of porosity. These are SC arrays (simple cubic packing), BCC arrays (body centred cubic packing), FCC arrays (faced centred cubic packing). First tests have been performed with $\omega = 0$, because previous static results [35] are available. Comparison of results is done on Fig. 6, plotting $H(\omega = 0)$ against the porosity n. We find a very good agreement except for very low porosity, for the FCC array. Nevertheless, the difference is always less than about 10%. For very low porosity, we need to use very fine grid, due to a very complex fluid flow. We can have better results in extrapolating those coming from a dynamic computation at low frequency (Fig. 7). The reason is perhaps that, in this case, the quantity $\int_{\Omega_l} \alpha_j^k \, d\Omega$ can be completly regularized.

Finally, we have checked the convergence of our computation on true 3D, dynamic cases. Let us just mention that no previous results were available for these cases. Figures 8a and b give respectively typical examples of a mesh for the SC and FCC arrays. They use all the possible symmetries. Figures 9 show a good convergence for the SC array with $n = 0.55$, using about 1000 elements. This means building, storing and solving a large linear system (1000 elements give 6000 degrees of freedom and a large and full matrix). We have obtained about the same convergence results for the other periodic arrays of spheres excepted for the FCC arrays with $n = 0.28$ and $n = 0.2595$. Figure 10 illustrates the convergence for the FCC array with $n = 0.2595$. The convergence of velocity and stress results for

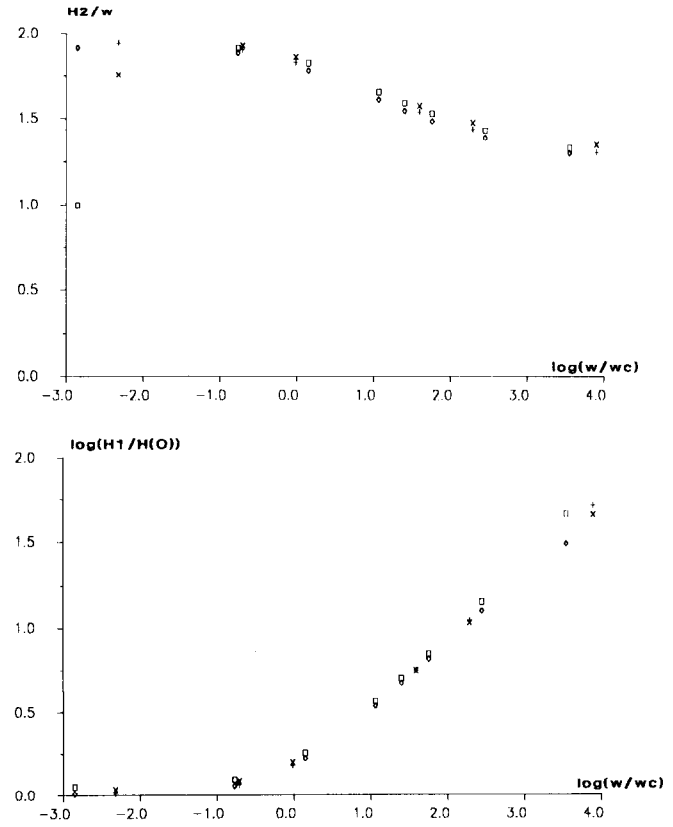

FIG. 9. SC array results, porosity $= n = 0.55$: +, fine mesh, 1038 elements velocity results; ×, fine mesh, 1038 elements stress results; ◇, coarse mesh, 715 elements velocity results; □, coarse mesh, 715 elements stress results.

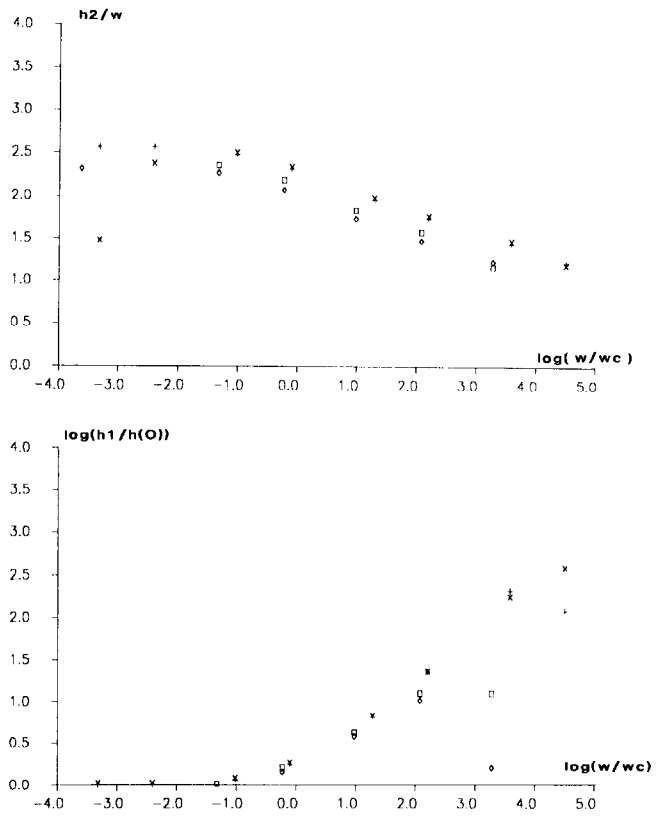

FIG. 10. FCC array results, porosity $= n = 0.2595$: +, fine mesh, 1122 elements velocity results; ×, fine mesh, 1122 elements stress results; ◇, coarse mesh, 832 elements velocity results; □, coarse mesh, 832 elements stress results.

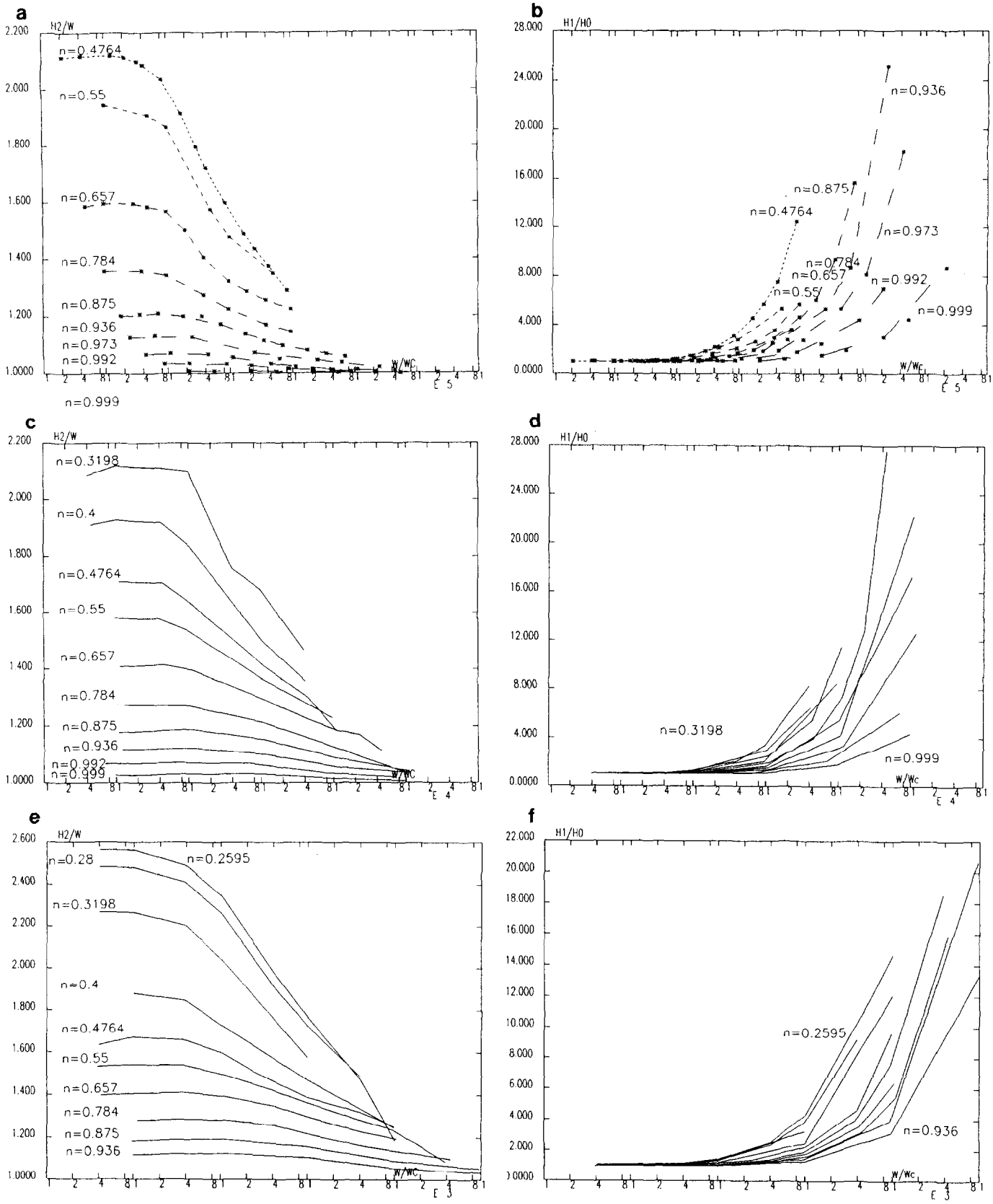

FIG. 11. Dynamic permeability for isotropic periodic arrays of spheres: (a), (b) simple cubic packing (SC); (c), (d) body centred cubic packing (BCC); (e), (f) faced centred cubic packing (FCC).

the finer grid provide good information on the accuracy of the computations. The memory space available does not allow us to perform computations on a finer grid to confirm the convergence in this last case.

In conclusion, these tests provide good results and illustrate the complementarity of velocity and stress methods, which give an estimate of the accuracy of the results. For the low frequency range ($\omega \ll \omega_c$), the velocity method gives accurate results. The stress method degenerates when ω decreases, a logical result, if we keep in mind that it does not work for $\omega = 0$. On the other hand, the stress method provides better results for the high frequency range than the velocity method. For high frequencies, fine meshes are required to obtain accurate results. When the frequency increases, the wavelength decreases, and we need to refine the mesh. This will lead us to practical limitations in the frequency range for more severe geometries.

4.2. Experiments

We now give, to our knowledge, new results. These are dynamic data for the previous isotropic arrays of spheres and for a 3D periodic array of connected ducts.

Isotropic Arrays of Spheres

As shown during the previous tests, convergence of stress and velocity methods can be achieved, except at high and low frequencies where respectively stress and velocity methods are the most accurate and converge with grid refinement. Figures 11 give these results for the isotropic periodic arrays of spheres. The asymptotic value for $nH2/\omega\rho = H2^{(a)}/\omega^{(a)}$, when ω tends to 0, does not exceed 2.6. Nevertheless, it varies from 1 to 2.6 along the porosity range.

As mentionned previously, for high frequencies, and mainly for low porosity, convergence with grid refinement is not always achieved. For obvious practical reasons, the size of the mesh cannot always follow the wavelength decrease. This leads to some lack of accuracy for high frequency results (curves crossing each other). Nevertheless, special efforts (computations on finer grids) have been made on given points to confirm the significant variations observed on $H(\omega)$, with the various 3D geometries. Despite the lack of accuracy for high frequencies, all curves $nH2/\omega\rho = f(\omega/\omega_c)$ seem to converge toward 1 when ω tends to infinity. It has been shown [1] that this limit value cannot be lower than 1, since we deal with isotropic arrays. The asymptotic study for high frequencies performed in [3] for 2D geometries could or could not confirm this result. Figures 11b, d, f also point out significant variations of $H1/H0$ with the porosity for the SC, BCC, and FCC arrays. Starting from $\omega/\omega_c = 1$, dynamic effects ($H1/H0 \neq 1$) are different for the various concentrations and arrays. These results give additional information for the scaling method for dynamic permeability in porous media proposed in [32]. But let us first remember this scaling method.

The main result of [32] is the following:

$$\frac{K(\omega)}{K(0)} = \tilde{K}\left(\frac{\alpha\omega}{\omega_c}\right).$$

$\tilde{K}$ is a function dominated by the geometry of the throat region in a medium. Assuming the pore cross sectional area to vary slowly near the throat, $\tilde{K}$ *can be approximated by a universal function independent of porous microstructures.*

α is the tortuosity coefficient. It is defined in [21] by the following asymptotic results, on which the scaling behavior [32] is based.

$K(\omega) = K(0) + iC_1(\omega\rho/\mu^2)$ when $\omega \to 0$

$K(\omega) = (in)/(\alpha\rho\omega)(1 - i(\delta/\lambda))$ when $\omega \to \infty$

C_1 is a coefficient with dimension of [area]^2.

λ is an effective pore-size of the medium.

$\delta = \sqrt{2\mu/\omega\rho}$

n is the porosity.

The link with our notations is simple:

$$\frac{na^2H2(\omega)}{2\mu}\Big/\frac{\omega a^2}{2v} = \frac{nH2(\omega)}{\omega\rho} = -\frac{nC_1}{\mu^2K^2(0)} \quad \text{when} \quad \omega \to 0$$

$$\frac{na^2H2(\omega)}{2\mu}\Big/\frac{\omega a^2}{2v} = -\alpha \quad \text{when} \quad \omega \to \infty$$

$$\frac{H1(\omega)}{H(0)} = \alpha\sqrt{2\mu K(0)/n\lambda^2}\sqrt{\omega/\omega_c} \quad \text{when} \quad \omega \to \infty.$$

Figures 12 show our previous BCC and FCC results under the form $K1(\omega)/K(0) = f_1(\omega/\omega_c)$, $K2(\omega)/K(0) = f_2(\omega/\omega_c)$, $|K(\omega)|/K(0) = f_3(\omega/\omega_c)$, Phase$(K(\omega)) = f_4(\omega/\omega_c)$, with $K(\omega) = K1(\omega) + iK2(\omega)$. The functions f_1, f_2, f_3, f_4 seems nearly the same for the various concentrations and arrays. At the opposite, the true physical parameters, $H1(\omega)/H(\omega = 0)$ representative of the viscous dissipative energy and $nH2(\omega)/\omega\rho$ representative of inertia effects (coupling mass), do not point out a similar universal behavior (Fig. 11).

Finally let us note that we have used ω/ω_c, instead of $\alpha(\omega/\omega_c)$ in [32]. This has no effect, since α seems to be equal to 1 for all the cubic packing tested. Moreover, Fig. 13 shows the same thing on two simple cylindrical arrays, where $\alpha = 1$ [3]. The scaling behavior [32] seems to be valid using K, but fails if we use $H = 1/K$. We could explain this deviation, using the more complete asymptotic

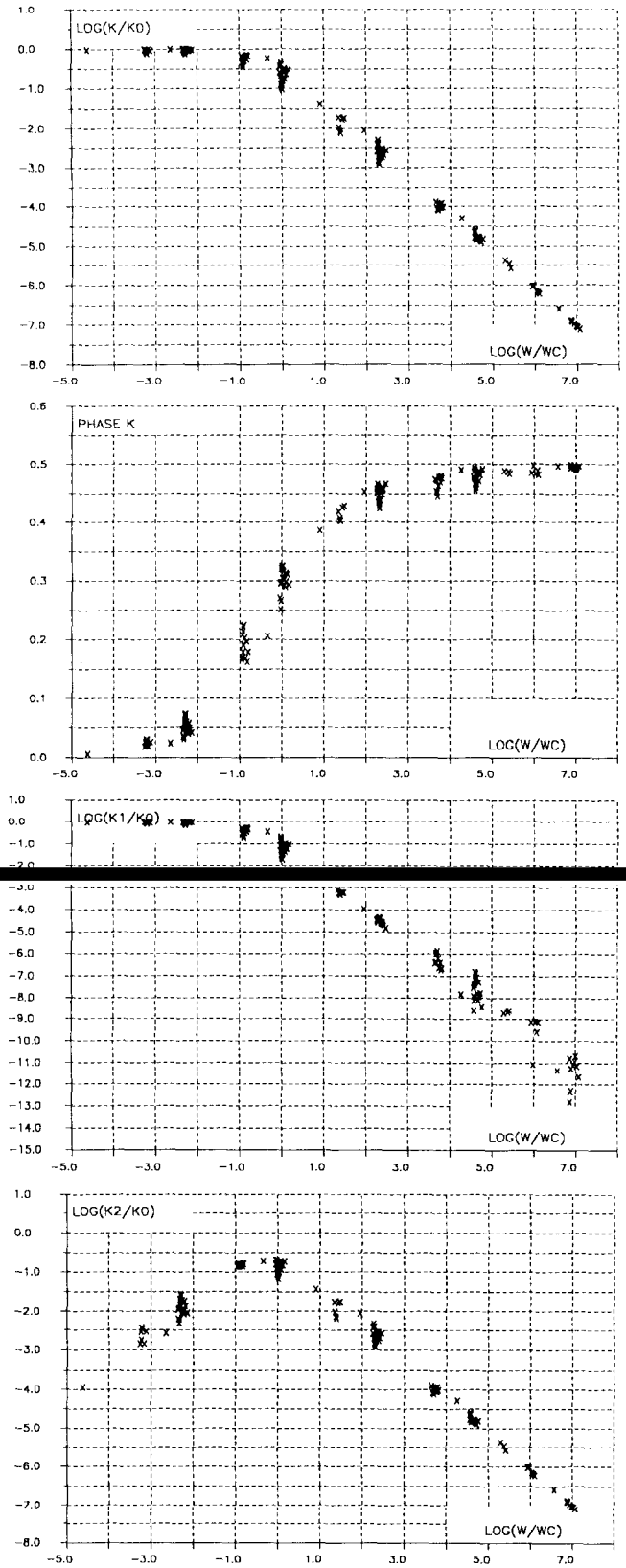

FIG. 12. Dynamic results using $K(w) = 1/H(w)$ for the BCC (body centred cubic packing), the FCC (faced centred cubic packing) arrays, and for various porosities.

frequency dependence when $\omega \to \infty$, given in [3, 13]. Providing asymptotic behavior of $H(\omega)$ gives us a physical explanation of the variations observed on $H(\omega)$. A first approximation was obtained assuming that, at high frequencies, the fluid is perfect (viscosity forces are negligible). Since the viscosity is zero at this initial step, the result concerned only the inertial part $H2$. And we obtained $nH2/\omega\rho = B^{-1}$ when $\omega \to \infty$, where in the general case B is a real symetrical tensor. The second approximation is given by the boundary viscous layer, itself considered as a plane layer in first approximation. This gives [3]

$$\frac{nH2}{\omega\rho} = B^{-1} + \sqrt{\mu/2\omega_c\rho}\, C \sqrt{\omega_c/\omega}$$

when $\omega \to \infty$

$$\frac{H1(\omega)}{H(0)} = \sqrt{\mu/2\omega_c\rho}\, C \sqrt{\omega/\omega_c}$$

when $\omega \to \infty$,

where C in the general case is a tensor, whose components are shape coefficient, the dimension of which is the inverse of a length. The first order on $H1$ gives a second order on $H2$. This asymptotic approximation is quite correct for $H2$ as shown on Fig. 13 in the simple cases of narrow slits or cylindrical ducts. But $H1$ needs a second order (Fig. 13); in fact a third-order approximation, which is constant, may be introduced, taking into account the curvature of the boundary layer. This may explain the deviation to the observed scaling behavior. For a given array, only the porosity is changed. This means that the radius of the spheres is changed, and also the curvature of the boundary layer. It clearly exhibits the role on the dynamic permeability of the curvature of the solid–fluid interface and the limits of the scaling behavior proposed in [32].

Dealing with $H1(\omega)/H(0)$ and $nH2(\omega)/\omega\rho$, the true physical parameters, it is not easy to find an approximate universal frequency dependance with a given number of geometric parameters. The asymptotic results on $H(\omega)$ with one order when $\omega \to 0$ and two orders when $\omega \to \infty$ give a good approximation. The transitional region, where low and high frequency approximations are not valid, is relatively reduced.

A 3D Periodic Array of Connected Ducts

Dealing with dynamic behavior of porous media, $H(\omega)$ is an essential parameter. Due to the lack of data, and the difficulty of measurements, authors have built models and made some assumptions to approximate $H(\omega)$, using analytical results obtained on smooth geometries. Our purpose is to consider the pore geometry of the period shown by MODEL3 of Fig. 14, and to check the validity of three

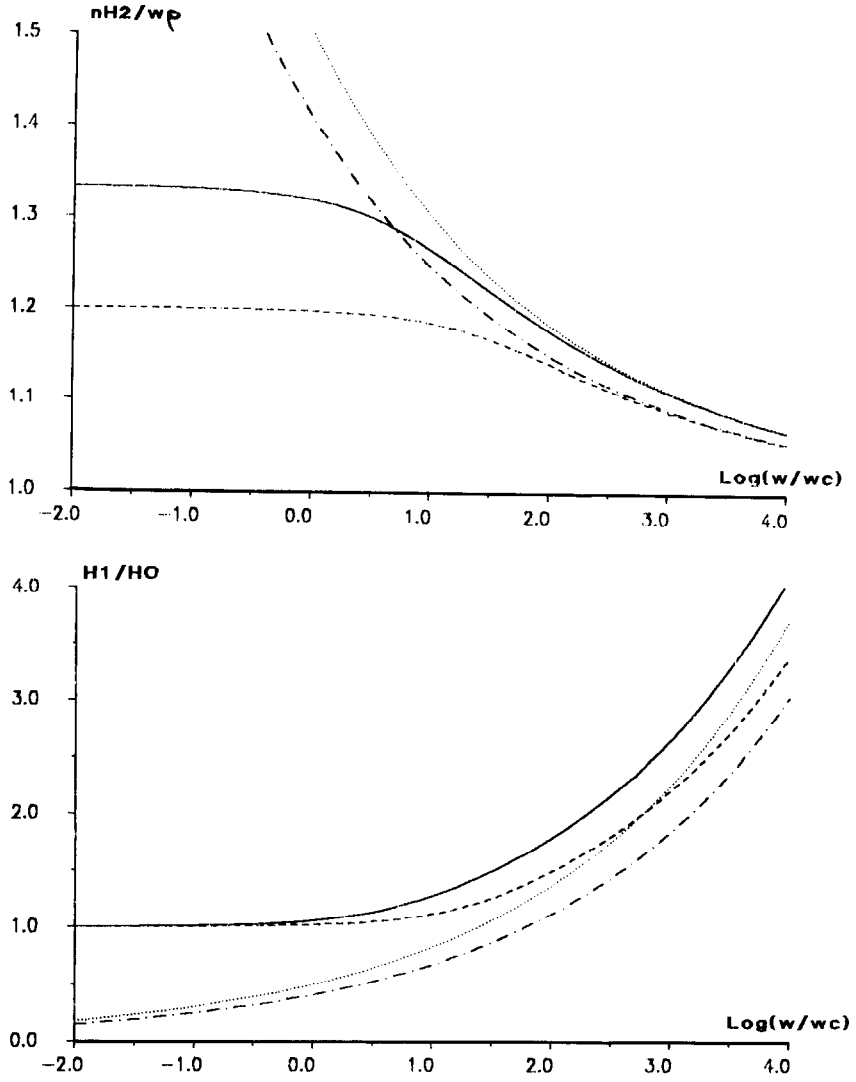

FIG. 13. Asymptotic behavior and scaling behavior on two very simple arrays: —, analytical results cylindrical ducts; ···, asymptotic behavior (3) cylindrical ducts; – – –, analytical results narrow slits; – · – ·, asymptotic behavior (3) narrow slits.

simplified models. Figure 15 gives the velocity and stress results we obtain using the three following models (Fig. 14):

MODEL1, the simplest model, is made of parallel cylindrical ducts in one direction. This is a monodimensional model, the simplest one. Corresponding analytical results are those used and referenced in the previous section 4.1.1.

MODEL2, the first refinement, uses cylindrical ducts in each direction without any interaction.

MODEL3, the second refinement, uses connected cylindrical ducts in each direction, assuming that the fluid in ducts orthogonal to the macroscopic pressure gradient do not play any role.

Boutin [16] shows how to deduce MODEL2 and MODEL3 from MODEL1.

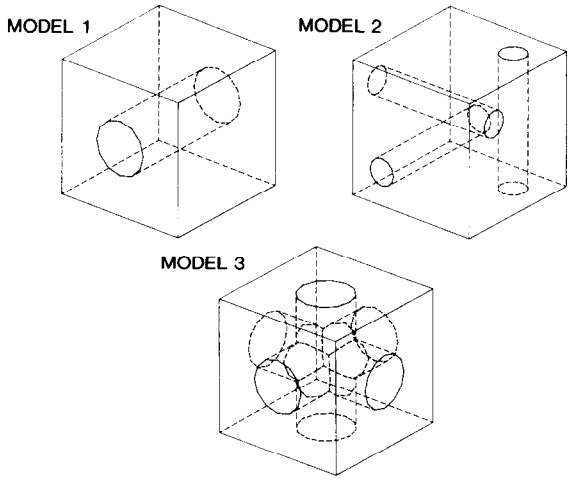

FIG. 14. Three approximated analytical models for a 3D array of connected cylindrical ducts.

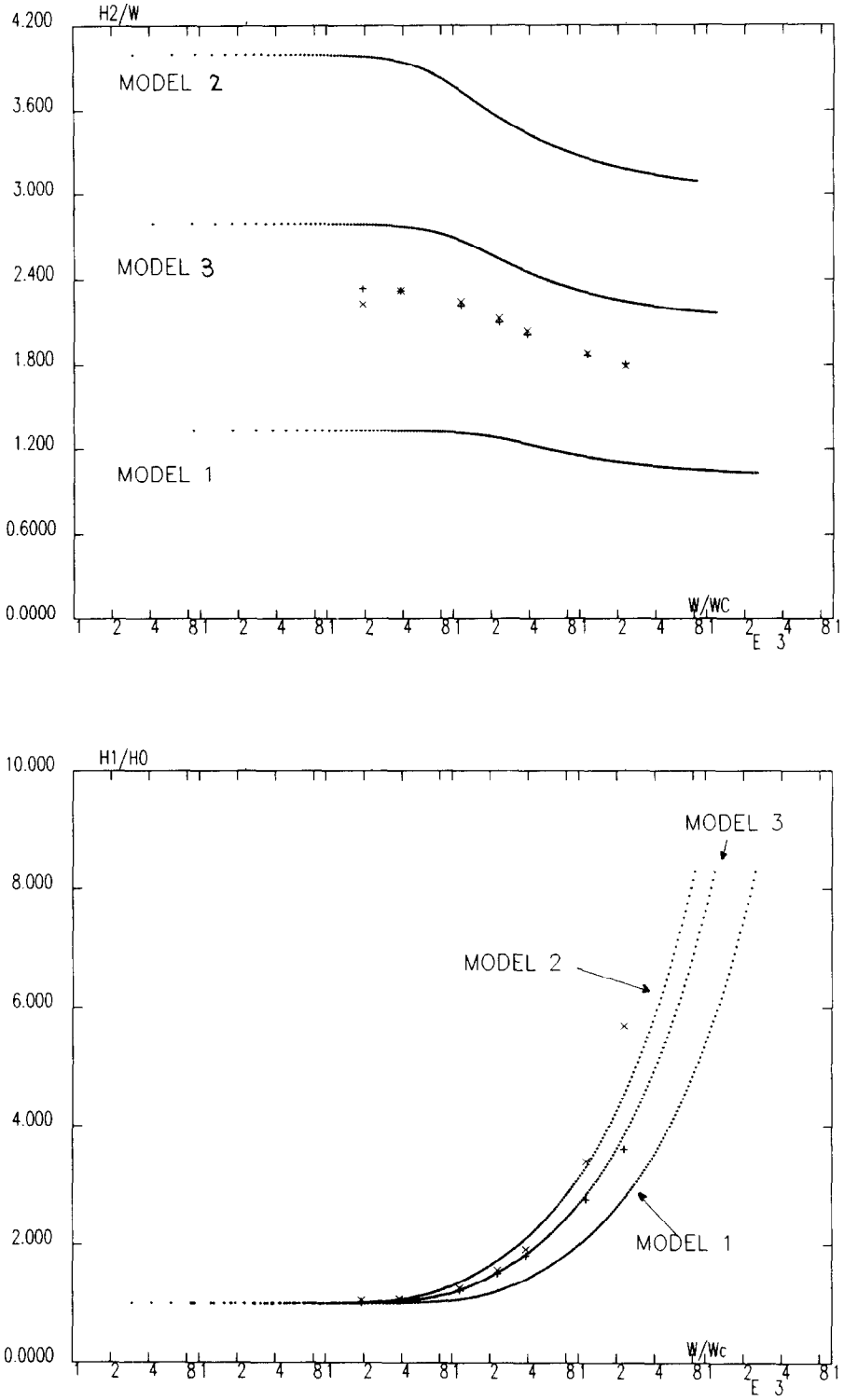

FIG. 15. Dynamic permeability for a 3D array of connected cylindrical ducts: +, velocity results; ×, stress results; ·, analytical results from models 1, 2, and 3; $H1(w)/H1(w=0)$ against w/wc; and $nH2(w)/wp$ against w/wc.

Logically, MODEL3 is confirmed as the best, despite an error of about 15% for $nH2/\omega\rho$. For high frequencies and for $H1$, the accuracy of our results do not allow us to compare MODEL2 and MODEL3, but the difference is also small.

5. CONCLUSIONS

The method presented provides encouraging results on a numerical side and quantitative results on a physical side. We could think of improving our results by using adapted integration schemes for high frequencies. Problems occur when the wave length of the Green kernel becomes of the order of magnitude of the mesh size. A method to use a periodic Green kernel could also improve the computations. In this case the velocity method would not be available, so the accuracy of a computation could not be checked by velocity and stress results.

Dealing with the dynamic behavior proposed for porous media, $H(\omega)$ is an important parameter. We have checked the scaling behavior proposed in [32] and shown its limits. Accurate measurements of $H(\omega)$ could also provide new geometrical information on the microstructure of a porous medium, such as an equivalent radius of curvature.

ACKNOWLEDGMENTS

The present work was started and mainly done when I was at the Institut de Mecanique de Grenoble. I wish to acknowledge Professor J. L. Auriault for initiating this work, Professor G. Bonnet and Dr. C. Boutin for fruitfull discussions. I also thank CERN (Geneva) where, as a fellow, I could achieve this work.

REFERENCES

1. J. L. Auriault, in *Two Medium Mechanics*, Summer school (Gdansk Polytechnic Institute, Gdansk, Poland, 1981).
2. J. L. Auriault, *Int. J. Eng. Sci.* **18**, 775 (1980).
3. J. L. Auriault, L. Borne, and R. Chambon, *J. Acoust. Soc. Am.* **77**, No. 5, 1641 (1985).
4. J. L. Auriault and E. Sanchez-Palencia, *J. Mec.* **16**, 575 (1977).
5. C. Avallet, Thesis, Institut de Mecanique de Grenoble, 1981 (unpublished).
6. A. Bensoussan, J. L. Lions, and G. Papanicolaou, *Asymptotic Analysis for Periodic Structures* (North-Holland, Amsterdam, 1978).
7. J. G. Berryman, *J. Acoust. Soc. Am.* **69**, 416 (1981).
8. M. A. Biot, *J. Acoust. Soc. Am.* **28**, 168 (1956).
9. M. A. Biot, *J. Acoust. Soc. Am.* **28**, 179 (1956).
10. M. A. Biot, *J. Appl. Phys.* **33**, 1482 (1962).
11. M. A. Biot, *J. Acoust. Soc. Am.* **34**, 1254 (1962).
12. M. A. Biot and D. C. Willis, *J. Appl. Mech.* **24**, 594 (1957).
13. L. Borne, Thesis, Institut de Mecanique de Grenoble, 1983 (unpublished).
14. L. Borne, R. Chambon, and J. L. Auriault, *Int. J. Num. Methods Fluids* **5**, 685 (1985).
15. L. Borne, *Int. J. Num. Methods Fluids* **7**, 581 (1987).
16. C. Boutin, Thesis, Institut de Mecanique de Grenoble, 1987 (unpublished).
17. H. D. Bui, B. Loret, and M. Bonnet, *C.R. Acad. Sci. Paris Ser. II* **300**, 14 (1985).
18. E. Charlaix, A. P. Kushnick, and J. P. Stokes, *Phys. Rev. Lett.* **61**, 1595 (1988).
19. N. C. Dutta, *Appl. Phys. Lett.* **37**, 898 (1981).
20. M. Hasimoto, *J. Fluid Mech.* **5**, 317 (1959).
21. D. L. Johnson, J. Koplik, and R. Dashen, *J. Fluid Mech.* **176**, 379 (1987).
22. D. L. Johnson, T. J. Plona, C. Scala, F. Pasierb, and H. Kojima, *Phys. Rev. Lett.* **49**, 1840 (1982).
23. V. D. Kupradze, *Three-Dimensional Problems of the Mathematical Theory of Elasticity and Thermoelasticity* (North-Holland, Amsterdam, 1979).
24. O. A. Ladyzhenskaya, *The Mathematical Theory of Viscous Incompressible Flow*. Gordon & Breach, London, 1969.
25. H. B. Li, G. M. Han, and H. A. Mang, *Int. J. Num. Methods Eng.* **21**, 2071 (1985).
26. J. C. Nedelec, Cours, Centre de Mathematiques Appliquees, Ecole Polytechnique 91128 Palaiseau Cedex, France, 1977 (unpublished).
27. T. J. Plona, *Appl. Phys. Lett.* **36**, 259 (1980).
28. E. Sanchez-Palencia, *Non-homogeneous Media and Vibration Theory*, Lecture Notes in Physics, Vol. 127 (Springer-Verlag, Berlin, 1980), Part II.
29. W. Schon and D. Salin, *J. Phys. Lett.* **42**, 477 (1981).
30. D. P. Schmitt, M. Bouchon, and G. Bonnet, in *55th Ann. Int. Seg. Meeting, Washington, DC, 1985.*
31. P. Sheng and M. Y. Zhou, *Phys. Rev. Lett.* **61**, 1591 (1988).
32. P. Sheng, M. Y. Zhou, E. Charlaix, A. P. Kushnick, and J. P. Stokes, *Physica A* **157**, 514 (1989).
33. C. H. Yew and P. N. Jogi, *J. Acoust. Soc. Am.* **60**, 2 (1976).
34. C. H. Yew and P. N. Jogi, *Exp. Mech.* **167** (1978).
35. A. A. Zick and G. M. Homsy, *J. Fluid. Mech.* **115**, 13 (1982).